



Effect of Al addition on oxidation behavior of Nb-based refractory alloys

Downloaded from: <https://research.chalmers.se>, 2025-12-15 16:31 UTC






Citation for the original published paper (version of record):

Li, X., Zhao, Y., Zhang, L. et al (2025). Effect of Al addition on oxidation behavior of Nb-based refractory alloys. AIP Advances, 15(4). <http://dx.doi.org/10.1063/5.0260885>

N.B. When citing this work, cite the original published paper.

RESEARCH ARTICLE | APRIL 07 2025

Effect of Al addition on oxidation behavior of Nb-based refractory alloys

Xiaolong Li ; Yufei Zhao ; Linwei Zhang; Qiang Hu; Huahai Mao ; Sheng Guo  

AIP Advances 15, 045012 (2025)

<https://doi.org/10.1063/5.0260885>

Articles You May Be Interested In

A review of refractory materials for vapor-anode AMTEC cells

AIP Conf. Proc. (January 2000)

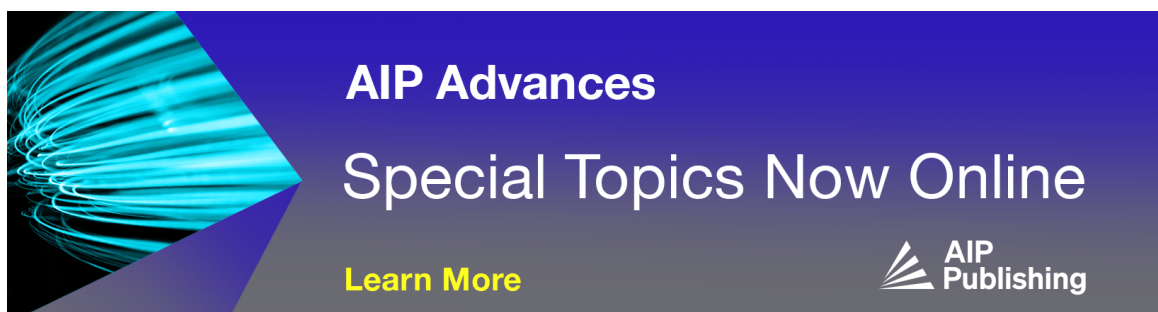
Solid solution softening or hardening induced by minor substitutional additions in a $\text{Hf}_{20}\text{Nb}_{31}\text{Ta}_{31}\text{Ti}_{18}$ refractory high entropy alloy

AIP Advances (August 2023)

The effect of hydrothermal curing on residual mechanical properties of refractory concrete


AIP Conf. Proc. (July 2018)

23 April 2025 14:22:41



AIP Advances
Special Topics Now Online

[Learn More](#)

 AIP Publishing

Effect of Al addition on oxidation behavior of Nb-based refractory alloys

Cite as: AIP Advances 15, 045012 (2025); doi: 10.1063/5.0260885

Submitted: 27 January 2025 • Accepted: 14 March 2025 •

Published Online: 7 April 2025



Xiaolong Li,¹  Yufei Zhao,¹  Linwei Zhang,² Qiang Hu,² Huahai Mao,³  and Sheng Guo^{1,a)} 

AFFILIATIONS

¹ Department of Industrial and Materials Science, Chalmers University of Technology, SE-41296 Gothenburg, Sweden

² Institute of Applied Physics, Jiangxi Academy of Sciences, Nanchang 330096, China

³ Thermo-Calc Software AB, Råsundavägen 18A, SE-16967 Stockholm, Sweden

^{a)} Author to whom correspondence should be addressed: sheng.guo@chalmers.se

ABSTRACT

The development of ultrahigh-temperature Nb-based refractory alloys is driven by the quest to further boost the energy efficiency of gas turbines. In terms of material requirements for ultrahigh-temperature applications, high strength at high temperatures, reasonable ductility at room temperature, and decent oxidation resistance are most critical. Unfortunately, meeting these three material requirements simultaneously is highly challenging, and in almost all scenarios, satisfying one requirement is at the cost of jeopardizing the other one or two. Comparatively, more research studies are dedicated to high-temperature strength, room-temperature ductility, and their trade-off, while less attention has been given to oxidation resistance. Here, in this work, improving the oxidation resistance of Nb-based refractory alloys is the focus. In particular, the effect of Al addition on the oxidation behavior of some newly developed Nb-based refractory alloys, Nb_{79.5-x}Hf₁₅W_{5.5}Al_x (x = 4, 8, 12, at. %), was investigated and benchmarked using the commercial WC3009 alloy. Noticeably, the oxidation resistance of these newly developed Nb-based refractory alloys is much superior to that of the benchmark WC3009 alloy. Although pitting is observed basically in all tested oxidation conditions, suggesting the formation of non-protective oxide scales, the oxidation resistance of Nb-based refractory alloys is significantly improved due to the beneficial effect of Al addition.

© 2025 Author(s). All article content, except where otherwise noted, is licensed under a Creative Commons Attribution-NonCommercial-NoDerivs 4.0 International (CC BY-NC-ND) license (<https://creativecommons.org/licenses/by-nc-nd/4.0/>). <https://doi.org/10.1063/5.0260885>

I. INTRODUCTION

Refractory alloys are natural candidates for ultrahigh-temperature applications, such as turbine engines, due to their inherent merits, including high melting points and high retained strength at elevated temperatures.¹⁻³ The energy efficiency of turbine engines is determined by the working temperature, and the higher the working temperature, the better the energy efficiency.⁴ The working temperature of the state-of-the-art Ni-based superalloys has, however, been limited by the relatively low melting point of nickel, the dominant element in them. Therefore, alternative materials with higher working temperature than those of Ni-based superalloys are in need. Due to processing considerations, metallically bonded refractory metals and alloys are more favored compared to covalently bonded ceramics or ordered intermetallic compounds. Out of refractory metals, Nb stands out with its high melting point of 2477 °C, low density of 8.58 g/cm³, and low

ductile-brittle transition temperature (DBTT) between -100 and -195 °C.⁵ Naturally, Nb-based refractory alloys have been given much attention in the pursuit of alternative ultrahigh-temperature materials.

For ultrahigh-temperature applications, high strength at high temperatures, reasonable ductility at room temperature, and decent oxidation resistance are three most critical material requirements. Meeting these three material requirements simultaneously is, however, a formidable task. Typically, satisfying one requirement is at the cost of jeopardizing the other one or two. Using Nb alloys as an example, Nb can be alloyed with other alloying elements (Si, for example) to achieve high strength and high oxidation resistance, but at the cost of much reduced room-temperature ductility.⁶ In general, among these three critical material requirements, oxidation resistance has received much less attention compared to the other two material requirements, i.e., high-temperature strength and room-temperature ductility. In addition, surface treatment like coating is

often utilized, instead of alloying, to protect alloys from oxidation, thus avoiding the trade-off between mechanical properties and oxidation resistance. Nevertheless, an acceptable oxidation resistance of the basement alloy is still needed in case the coating fails.⁷

In some commercial Nb-based refractory alloys, the improvement in oxidation resistance relies on the addition of Ti,⁸ which is apparently not good enough. Meanwhile, it is well known that the formation of compact and continuously protective oxide scales, such as Al_2O_3 , Cr_2O_3 , and SiO_2 , is effective in providing oxidation resistance, in comparison with the partially protective TiO_x scale and those non-protective refractory oxide scales. In particular, Al_2O_3 is often considered the most effective protective scale since it can be thermodynamically stabilized up to 1400°C without any concern on volatility.⁹ However, the introduction of Al into the Nb-based alloys could adversely affect their high-temperature strength and/or room-temperature ductility. The amount of Al addition needs to be carefully controlled to maintain a balance of mechanical properties and oxidation resistance. Here, in this work, we modified a commercial Nb-based refractory alloy, WC3009 (Nb-30Hf-9W, wt. %, or $\text{Nb}_{79.5}\text{Hf}_{19.2}\text{W}_{5.6}$, at. %) and developed a $\text{Nb}_{79.5-x}\text{Hf}_{15}\text{W}_{5.5}\text{Al}_x$ ($x = 4, 8, 12$, all in at. %) alloy system. WC3009 was selected as the benchmark alloy due to its good tensile ductility at room temperature and its ability to retain high strength up to 1200°C .¹⁰ Compared to WC3009, we almost kept the same amount of W due to its strong solid solution strengthening effect (especially at elevated temperatures), reduced the content of Hf by around 5 at. % in order to allow Al addition without jeopardizing the room-temperature ductility, and then added Al up to 12 at. % so as to improve the oxidation resistance while maintaining the single-phase bcc structure of the developed alloys. The main objective of this work is to study the role of Al addition on the oxidation behavior of these newly developed Nb-based alloys, assuming that they exhibit similar room-temperature ductility and high-temperature strength to those of WC3009.

II. EXPERIMENTAL

Nb-based refractory alloys with nominal compositions $\text{Nb}_{79.5-x}\text{Hf}_{15}\text{W}_{5.5}\text{Al}_x$ ($x = 4, 8$, and 12 , at. %, with alloys denoted as 4Al, 8Al, and 12Al afterward) and the benchmark WC3000 alloy were produced by the arc melting of high purity (>99.95%) elements at least 5 times to ensure chemical homogeneity followed by drop casting, with ingots having cross section dimensions of $10 \times 10 \text{ mm}^2$. Microstructure and chemical compositions were examined using a field emission gun scanning electron microscope (FEG-SEM, LEO-1550) equipped with a backscattered electron (BSE) detector, an energy dispersive spectrometer (EDS), and an electron backscatter diffractometer (EBSD). Compositional analysis from SEM-EDS is provided in Table I. There were some losses of Al due to its low boiling point of 2470°C compared to the melting points of those refractory metals, during the repeated arc melting process. The crystal structure was examined using an x-ray diffractometer (XRD, Bruker D8 Advance), using $\text{Cu-K}\alpha_1$ radiation in the 2θ range of 20° – 100° (20° – 80° for oxidized specimens). The Vickers hardness (Struers DuraScan-70 G5) at room temperature was tested under a load of 5 kgf for a duration of 15 s. The hardness values were averaged out from over 20 indentations and are listed in Table I as well. WC3009 has the lowest hardness of 278 (HV5),

TABLE I. EDS measured compositions (at. %) of the Nb-based refractory alloys and the Vickers hardness (HV5) at room-temperature.

Alloy ID	Nb	Hf	W	Al	Hardness
WC3009	75.3	19.7	5.0	...	278 ± 5
4Al	75.6	15.1	5.8	3.5	317 ± 5
8Al	70.3	17.5	4.5	7.6	357 ± 6
12Al	67.3	15.9	5.0	11.9	423 ± 11

and hardness increases with the increasing of Al content up to 423 (HV5) for the 12Al alloy. Oxidation tests for the target alloys were carried out in a tube furnace pre-heated to 800 , 1000 , and 1200°C , respectively, for durations of 1, 8, and 24 h in static laboratory air. When the time was due, the sample was removed from the furnace and cooled in the air. The specimens for oxidation tests were in the form of cubic blocks with approximate dimensions of $4 \times 4 \times 4 \text{ mm}^3$. Before the oxidation tests, the surfaces of each specimen were ground to 1200-grit finish, ultrasonically cleaned in the ethanol, and air dried. The surface area (including all six faces) was accurately calculated by carefully measuring the dimensions of each specimen. The specimen was loaded in a crucible with dimensions of $20 \times 20 \times 20 \text{ mm}^3$, and the crucible with the specimen inside was weighed before and after the oxidation tests, using a highly sensitive balance (to the precision of 10^{-6} g) to evaluate the weight change. To prevent any loss of oxidation products during the oxidation tests and/or cooling in the air, an alumina lid was placed to cover the crucible throughout the oxidation and weighing process. Finally, the specific mass change was determined, dividing the measured mass change by the initial surface area of the specimen.

III. RESULTS AND DISCUSSION

Figure 1 shows the grain size distribution of the WC3009, 4Al, 8Al, and 12Al alloys from the EBSD analysis. The average grain size of the WC3009 alloy is $30.64 \mu\text{m}$. The grain size of $\text{Nb}_{79.5-x}\text{Hf}_{15}\text{W}_{5.5}\text{Al}_x$ alloys gradually decreases with the increasing Al content, from 4Al to 12Al: the average grain size of the 4Al sample is the largest, reaching $44.52 \mu\text{m}$, while the average grain size of the 12Al sample is the smallest, reaching $36.87 \mu\text{m}$. The bar chart further shows that the grain size distribution also changes with increasing Al content. The grain size distribution of the 12Al sample is the most concentrated, which means that the grain size is more uniform. The grain size distribution of 4Al and 8Al samples is relatively broad, especially the 4Al sample, showing a larger grain size distribution range. The increase in Al content leads to grain refinement, which may be because the increasing Al content limits the growth kinetics of the grains and thus forms a finer grain structure. In addition, a reduction in grain size contributes to an increase in the material's yield stress (in addition to the solid solution strengthening effect due to Al), which is also consistent with the trend observed in the hardness test results. A typical EDS elemental mapping from the 8Al alloy, presented in Fig. 2, shows dendritic and inter-dendritic features, with the segregation of Nb and W with high melting points in the dendritic region, while Hf and Al with relatively low melting points in the inter-dendritic region. Similar patterns of elemental

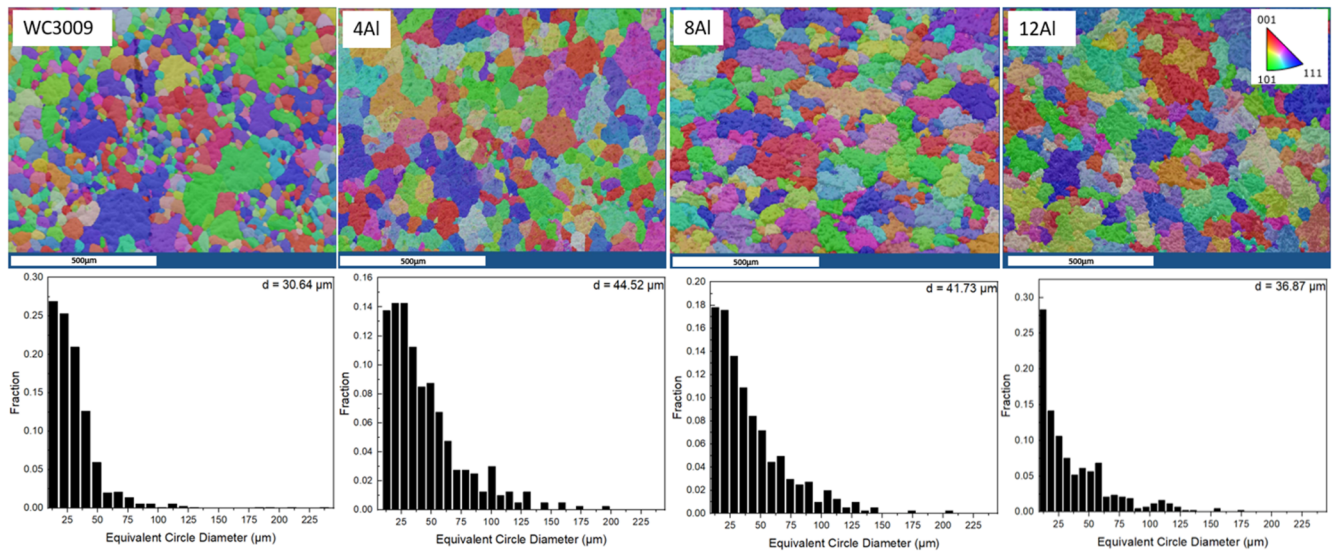


FIG. 1. EBSD results of the Nb-based refractory alloys with their grain size distributions in the as-cast condition.

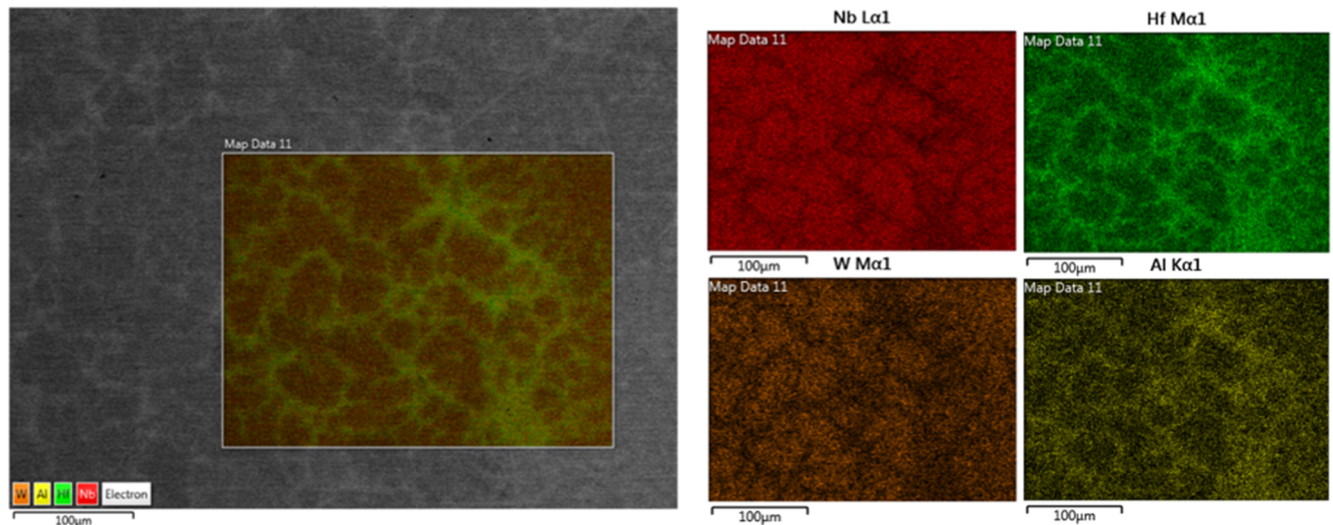


FIG. 2. Elemental mapping of the 8Al alloy.

distribution were seen in all alloys tested and are not shown here for simplicity.

WC3009, 4Al, and 8Al are identified to be of the single-phase bcc structure, while a small peak around $2\theta = 26.7^\circ$ corresponding to the ordered B2 phase is seen in 12Al alloy, according to Fig. 3. With an increased amount of Al addition from 4, 8 to 12 at. %, peaks are slightly shifted to the right, indicating a reduction in the lattice parameter due to the smaller atomic size of Al compared to those of refractory metal elements. For the WC3009 alloy, peaks are slightly shifted to the left compared to those of the 4Al alloy, indicating its

larger lattice parameter due to the higher content of Hf and Nb with larger atomic size (Hf 155 pm and Nb 146 pm).

Figure 4 shows how the oxidized samples look after they were removed from the furnace where the oxidation studies were done. It can be observed that except for the specimens oxidized at 800°C for 1 h, which have no obvious pitting (disintegration into powder), all the other specimens show pitting to different degrees. Two trends are obvious even before the oxidation kinetics analysis. First, the volume of spalled-off materials increases significantly with the increase in oxidation time. Second, with the increase in Al content,

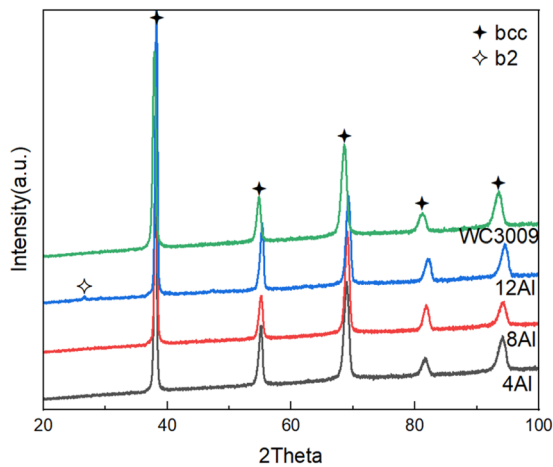


FIG. 3. XRD pattern of the Nb-based refractory alloys in the as-cast condition.

the volume of the spalled-off materials obviously decreases. The oxidation resistance is much improved for the alloys with higher than 8 at.% addition of Al. For the WC3009 alloy, the oxidation products experience a color change: from primarily black at 800 °C to

greenish at 1000 °C, and finally to greenish and yellowish at 1200 °C. For $\text{Nb}_{79.5-x}\text{Hf}_{15}\text{W}_{5.5}\text{Al}_x$ alloys, the oxidation products in 800 °C oxidized specimens appear as a fine black powder, while for samples oxidized at 1000 and 1200 °C, the oxidation products appear primarily black and yellow and require some grinding work to turn into powder.

The diagrams in Fig. 5 show the oxidation kinetics curves of specimens at 800, 1000, and 1200 °C, respectively. The oxidation kinetics were also quantified, following the growth rate law,

$$\frac{\Delta m}{SA} = kt^n, \quad (1)$$

where Δm is the mass change in mg, SA is the initial surface area, and $\frac{\Delta m}{SA}$ is the specific mass change normalized by the initial total surface area with the unit of mg/cm^2 , k is the rate constant, t is the oxidation time, n is the time exponent, and R^2 indicates the quality of the fitting. The rate constants k are dependent on n , so they cannot be directly compared with different n values. The time exponents n can, however, be compared directly among different alloys, and they indicate different active oxidation mechanisms. The fitting results are summarized in Table II. At all three temperatures, it can be observed that the largest mass gain is with the WC3009 alloy followed by the 4Al alloy, and the smallest mass gain is with the 12Al

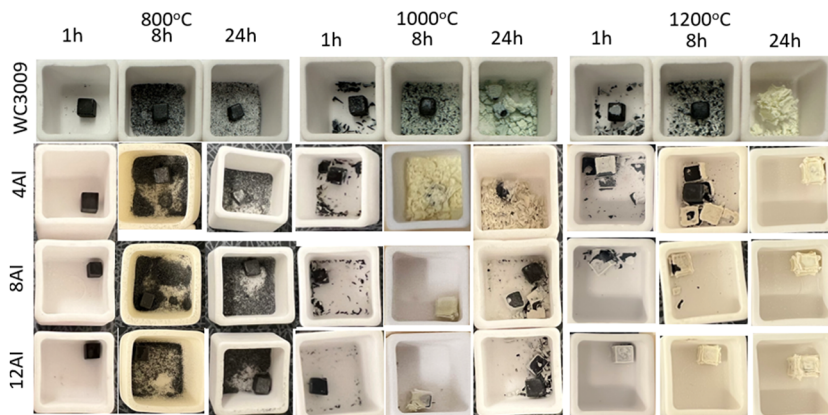


FIG. 4. Optical images of the oxidized specimens at 800, 1000, and 1200 °C after 1, 8, and 24 h of exposure, respectively, with the crucible dimensions of $20 \times 20 \times 20 \text{ mm}^3$.

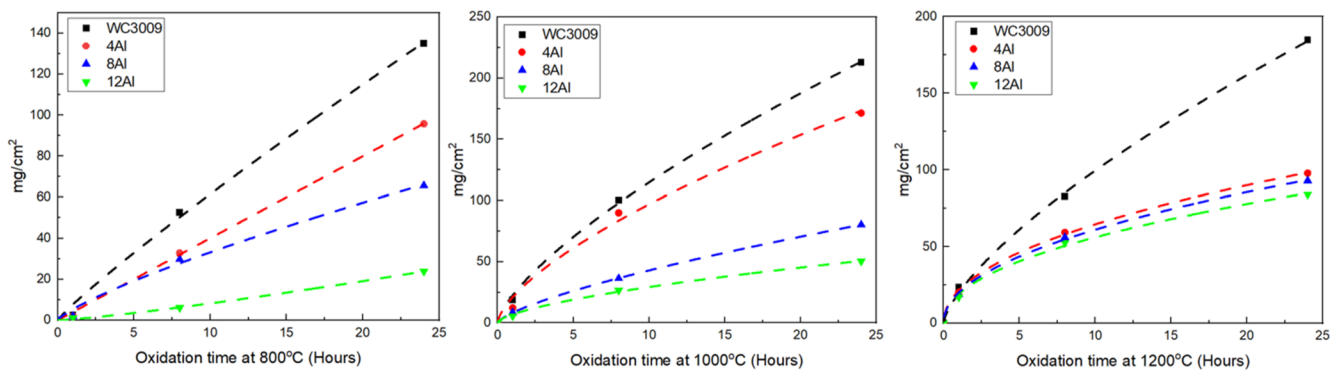


FIG. 5. Oxidation kinetics of the Nb-based refractory alloys at 800, 1000, and 1200 °C.

TABLE II. Summarized fitting parameters for oxidation kinetics analysis at 800, 1000, and 1200 °C.

Alloy ID	k (mg cm ⁻² h ⁻ⁿ)	n	R^2
T = 800 °C			
WC3009	7.70 ± 2.42 (5.68 ± 0.29)	0.90 ± 0.10 (1)	0.9962 (0.9948)
4Al	4.03 ± 0.77 (4.03 ± 0.07)	1.00 ± 0.06 (1)	0.9989 (0.9993)
8Al	5.40 ± 2.01 (2.74 ± 0.26)	0.79 ± 0.12 (1)	0.9922 (0.9823)
12Al	0.50 ± 0.16 (0.99 ± 0.06)	1.21 ± 0.11 (1)	0.9982 (0.9925)
T = 1000 °C			
WC3009	22.45 ± 2.52	0.71 ± 0.04	0.9990
4Al	21.01 ± 6.67	0.66 ± 0.11	0.9904
8Al	8.27 ± 0.21	0.72 ± 0.01	1
12Al	6.92 ± 1.19	0.63 ± 0.06	0.9965
T = 1200 °C			
WC3009	19.76 ± 2.69	0.70 ± 0.05	0.9984
4Al	20.33 ± 1.90	0.50 ± 0.03	0.9978
8Al	18.81 ± 2.01	0.51 ± 0.04	0.9973
12Al	17.31 ± 3.01	0.51 ± 0.06	0.9925

alloy. This clearly indicates that the increase in Al contents improves the oxidation resistance of the alloys. The 12Al alloy has the lowest oxidation rate at all temperatures and exhibits the best oxidation resistance.

The fitting curves at 800 °C show a gradually increased weight gain over time and a gradually decreased weight gain with increased Al additions. This general trend is also seen at 1000 and 1200 °C. Because of the Al additions, the weight gain is lowered from 135 mg/cm² for WC3009 to around 24 mg/cm² for 12Al after 24 h of oxidation, being consistent with the optical images shown in Fig. 4. The oxidation kinetics appears linear, i.e., n is close to 1. To reflect the seen oxidation behavior more reasonably, n was fixed to 1, and the oxidation coefficient k and the coefficient of determination R^2 were recalculated. The newly obtained fitting results are shown in brackets in Table II. With linear oxidation kinetics, the oxidation process is controlled by the interface reaction, and the oxygen reacts directly with the sample surface to form an oxide layer, but this layer is thin and does not significantly hinder further oxidation. According to Fig. 4, there is an obvious peeling phenomenon on the specimens oxidized at 800 °C for 8 and 24 h, and the oxidation products present as black powders. It can be inferred that at this temperature, the formation of oxides cannot effectively block the diffusion of oxygen. The k values show a gradually decreasing trend with more Al additions, when n was fixed to 1. The change in k values can be rationalized by the Pilling–Bedworth ratio of alloying elements: 2.69 for Nb and 3.35 for W, while it is 1.62 for Hf and 1.28 for Al,¹¹ so the addition of Al alleviates the spalling-off tendency of oxides with the Pilling–Bedworth ratio >2.

The oxidation curve at 1000 °C begins to show a seemingly parabolic law trend ($n < 1$, in the range of 0.63–0.72), i.e., the oxidation rate gradually slows down over time. This is due to the gradual

thickening of the oxide layer, which hinders the penetration of oxygen and other diffusers (e.g., nitrogen), and the oxidation process begins to be dominated by diffusion control. It can be seen from Fig. 4 that the oxidation products of the sample at 1000 °C contain black powders and yellow flakes. The occurrence of oxides spalling off indicates that the oxide layer is thick but brittle. The weight gain decreases from 213 mg/cm² for WC3009 to 50 mg/cm² for 12Al after 24 h of oxidation. The k values show a sharp decrease from around 21–22 for WC3009 and 4Al to around 7–8 for 8Al and 12Al with comparable n values.

For Nb_{79.5–x}Hf₁₅W_{5.5}Al_x alloys, the oxidation curve at 1200 °C follows the parabolic law and has smaller n values (~0.5) than those at 1000 °C. At relatively high temperatures, the initial oxidation is fast, generating a large amount of oxidation products. With the extension of time, the oxide layer rapidly becomes thicker, which slows down further oxidation reactions, resulting in a decrease in the oxidation rate. The oxidation products of the specimens appear as a large amount of black and yellow flake-shaped materials, which needed to be ground to become powders. Compared to the case of 1000 °C, the oxide layer formed at such high temperatures is thicker and more difficult to spall off. The weight gain is slightly decreased from 98 mg/cm² for 4Al to 93 mg/cm² for 8Al and then to 84 mg/cm² for 12Al, after 24 h of oxidation. From the fitting parameters, n is about 0.5, and the k values slightly decrease with increasing Al additions, with n being roughly the same. The oxidation behavior of WC3009, however, is quite different at this temperature compared to those of Nb_{79.5–x}Hf₁₅W_{5.5}Al_x alloys: the weight gain is 185 mg/cm² after 24 h of oxidation, much higher than that of 4Al; n is about 0.7, close to the value at 1000 °C; its oxidation rate is much faster compared to those of Nb_{79.5–x}Hf₁₅W_{5.5}Al_x alloys, and oxides almost fully disintegrate into powder after 24 h

23 April 2025 14:22:41

of oxidation. Apparently, the beneficial effect of Al addition to oxidation resistance is the most obvious at 1200 °C.

The XRD patterns of oxides formed at 800, 1000, and 1200 °C for 8 h are shown in Fig. 6, and the results are summarized in Table III. It is noted here that the types of oxidation products are almost the same after different oxidation exposure time (4, 8, and 24 h) at the same temperature, although their contents differ. Therefore, only the results for 8 h are shown here. The types of oxides that appear in the WC3009 alloy are the same, Nb₂O₅, Hf₆Nb₂O₁₇, and WO₃, but with different crystal structures at different temperatures. The similar scenario goes for the Nb_{79.5-x}Hf₁₅W_{5.5}Al_x alloys, but exceptions are with those Al-containing complex oxides. Nb₂O₅ as the main oxide is kinetically favored in all these alloys, where Nb is the dominant element. The crystal structure of Nb₂O₅, however, changes from orthorhombic at 800 °C to monoclinic at 1000 and 1200 °C. When Nb alloys are alloyed with 15–20 at. % of Hf, as is the case of target alloys here in this work, a complex oxide Hf₆Nb₂O₁₇ can be identified, although many of its peaks overlap with that of HfO₂. Its formation could be a solid-state reaction between HfO₂ and Nb₂O₅ by annealing at high temperature (6HfO₂·Nb₂O₅), similar to the formation of Hf₆Ta₂O₁₇.^{12,13} Its oxidation resistance is

better than the exclusive formation of HfO₂ and Nb₂O₅, and once it forms, it helps slow down the oxidation rate. It maintains the orthorhombic crystal structure at all these three temperatures. With 4.5–5.8 at. % of W addition in these alloys, WO₃ is formed with a transition of crystal structure from hexagonal at 800 °C, to monoclinic at 1000 °C, and then to a mixture of monoclinic and tetragonal at 1200 °C. Tetragonal WO₃ is favorably formed at high temperatures, and the monoclinic form is the most favorable one at low temperatures. Here, after 8 h of exposure to oxidation in laboratory air followed by a quick take-out for air cooling, it is possible that some tetragonal WO₃ could be preserved to room temperature. As for the Nb_{79.5-x}Hf₁₅W_{5.5}Al_x alloys with 4, 8, and 12 at. % of Al addition, AlNbO₄ with the monoclinic structure is formed at 800 and 1000 °C, while Nb₁₁AlO₂₉ with also the monoclinic structure is formed at 1200 °C. Both these Al-containing complex oxides display a more protective nature than Nb₂O₅.^{14,15}

From the seen oxidation products at different temperatures, it is found that increasing temperature results in the emergence of some new phases that are relatively difficult to form at low temperatures and phase transitions of some existing phases (e.g., from orthorhombic Nb₂O₅ to monoclinic Nb₂O₅ and from hexagonal

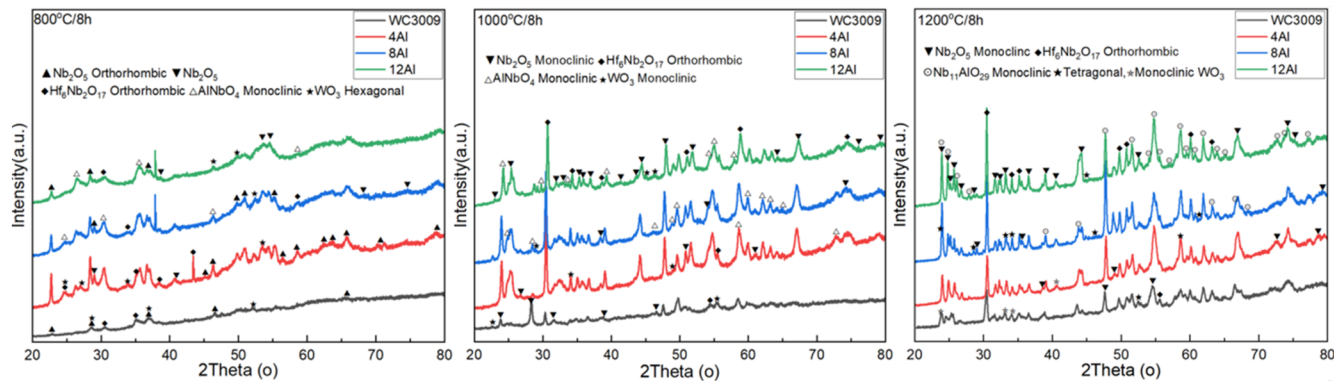


FIG. 6. XRD patterns after 8 h of oxidation exposure for the Nb-based refractory alloys at 800, 1000, and 1200 °C.

TABLE III. Summarized oxidation products after 8 h of exposure for the Nb-based refractory alloys at 800, 1000, and 1200 °C.

Alloy ID	Oxidation products
800 °C/8 h	
WC3009	Nb ₂ O ₅ (orthorhombic), Hf ₆ Nb ₂ O ₁₇ (orthorhombic), WO ₃ (hexagonal)
4Al, 8Al, 12Al	Nb ₂ O ₅ (orthorhombic), Hf ₆ Nb ₂ O ₁₇ (orthorhombic), AlNbO ₄ (monoclinic), WO ₃ (hexagonal)
1000 °C/8 h	
WC3009	Nb ₂ O ₅ (monoclinic), Hf ₆ Nb ₂ O ₁₇ (orthorhombic), WO ₃ (monoclinic)
4Al, 8Al, 12Al	Nb ₂ O ₅ (monoclinic), Hf ₆ Nb ₂ O ₁₇ (orthorhombic), AlNbO ₄ (monoclinic), WO ₃ (monoclinic)
1200 °C/8 h	
WC3009	Nb ₂ O ₅ (monoclinic), Hf ₆ Nb ₂ O ₁₇ (orthorhombic), WO ₃ (tetragonal, monoclinic)
4Al, 8Al, 12Al	Nb ₂ O ₅ (monoclinic), Hf ₆ Nb ₂ O ₁₇ (orthorhombic), Nb ₁₁ AlO ₂₉ (monoclinic), WO ₃ (tetragonal, monoclinic)

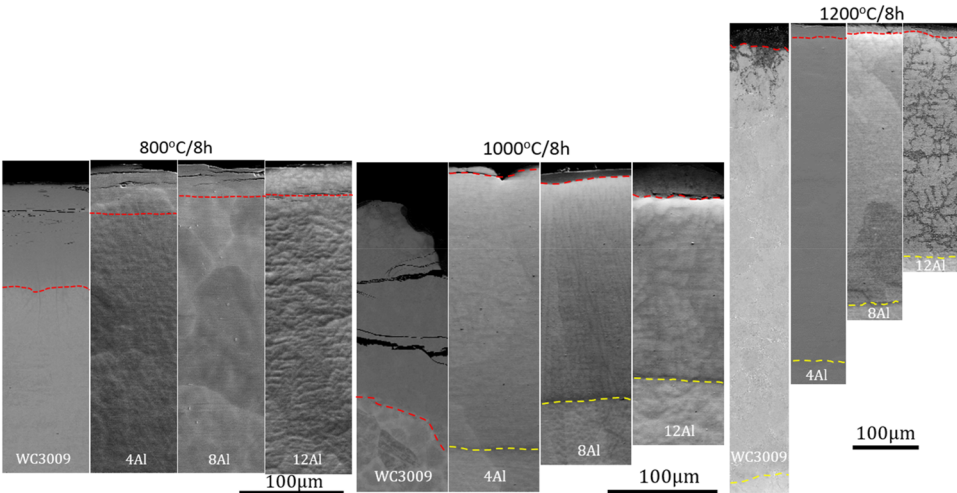


FIG. 7. Backscattered electron images of cross sections of the Nb-based refractory alloys after 8 h of oxidation exposure at 800, 1000, and 1200 °C. Oxide scales are at the top, separated from the base refractory alloy or the transition layer by red dashed lines, and transition layers are located between the base refractory alloy and the oxide scale, separated from the base alloy by yellow dashed lines.

TABLE IV. Thickness of the oxide layer (t_{oxide}) and the transition layer ($t_{\text{transition}}$), measured for 8 h oxidized specimens from Fig. 7.

	t_{oxide}	$t_{\text{transition}}$	t_{oxide}	$t_{\text{transition}}$	t_{oxide}	$t_{\text{transition}}$	t_{oxide}	$t_{\text{transition}}$
Temperature	WC3009		4Al		8Al		12Al	
800 °C	103 μm	...	45 μm	...	27 μm	...	25 μm	...
1000 °C	187 μm	...	9 μm	246 μm	12 μm	186 μm	30 μm	118 μm
1200 °C	25 μm	619 μm	20 μm	470 μm	13 μm	397 μm	15 μm	309 μm

WO₃ to monoclinic and tetragonal WO₃). In particular, the formation of AlNbO₄ and Nb₁₁AlO₂₉ phases is more obvious in the specimens with higher Al contents, indicating that the addition of Al plays an important role in forming different Al-containing complex oxides, contributing to slowing down the oxidation process and the resultant better oxidation resistance. The change of crystal structure and/or types of oxides may be the reason for the color change of oxidation products shown in Fig. 4. It is noted here that efforts trying to reveal the distribution of various oxides with reference to the base refractory alloy and hence to establish a correlation with XRD results by EBSD phase mapping were unfortunately unsuccessful due to these oxides failing to form a continuous layer/phase and their small size.

The backscattered electron images presented in Fig. 7 show cross-sectional observations of all specimens after 8 h of oxidation at three temperatures with different Al contents. At 800 °C, no distinction between the oxide layer and the transition layer is observed in all specimens, indicating that the oxidation process is a direct reaction between alloys and oxygen corresponding to the interface-controlled diffusion, leading to linear oxidation behavior. At 1000 °C, the WC3009 specimen also shows no obvious distinction between the oxide layer and the transition layer, while the 4Al, 8Al, and 12Al specimens show a clear distinction between these two. For the WC3009 specimen, as seen from Fig. 4, on its appearance after oxidation indicating obvious peeling, it can be inferred that the oxide layer is almost completely spalled off. The higher Al content

helps enhance the oxide layer adhesion to the material underneath, and therefore, some oxide layer remains to be seen on top of the transition later in the 4Al, 8Al, and 12Al specimens. At 1200 °C, all specimens show a clear distinction between the oxide layer and the transition layer.

It can be observed that the thickness of the transition layer (summarized in Table IV) increases with the increase in temperature and the decrease in Al content. Less can be concluded regarding the thickness of the oxide layer though, due to their spalling off. Therefore, it appears that adding Al up to 12 at.% helps improve oxidation resistance; it is, however, not sufficient to form a dense and protective oxide layer, e.g., the expected Al₂O₃ layer or a complex oxide layer that is sufficiently protective.

IV. CONCLUSIONS

The following conclusions can be drawn from the findings of this work:

1. The newly developed Nb-based refractory alloys, 4Al, 8Al, and 12Al, and the benchmark WC3009 alloy, all show a single-phase bcc structure with a typical dendritic structure, where Nb and W are enriched in the dendrite regions and Hf and Al are enriched in the inter-dendritic regions. Ordering is seen in the 12Al alloy. The Vickers hardness monotonously increases with the increasing Al content.

2. The oxidation resistance of the newly developed alloys is much superior to the WC3009 alloy. Except for the condition for oxidation at 800 °C for 1 h, peeling is observed in all alloys. Peeling becomes more significant at higher temperatures and with longer exposure durations. The increase in Al content reduces the severity of peeling, which is, however, not fully suppressed.
3. The oxidation kinetics of the alloys experiences a transition from the linear behavior at 800 °C to semi-parabolic at 1000 °C and then to parabolic at 1200 °C. Therefore, the controlling mechanism of the oxidation process shifts from interfacial reaction at 800 °C to diffusion at 1000 and 1200 °C.
4. Complex oxides are generated upon oxidation at different temperatures, including orthorhombic $\text{Hf}_6\text{Nb}_2\text{O}_{17}$, monoclinic AlNbO_4 , and monoclinic $\text{Nb}_{11}\text{AlO}_{29}$. The crystal structure of oxides transforms with increasing temperature, e.g., from orthorhombic Nb_2O_5 to monoclinic Nb_2O_5 and from hexagonal WO_3 to monoclinic and tetragonal WO_3 . Meanwhile, the change of oxide types is also observed at different temperatures, e.g., from monoclinic AlNbO_4 at 800 and 1000 °C to monoclinic $\text{Nb}_{11}\text{AlO}_{29}$ at 1200 °C.
5. At 800 °C, no distinction between the oxide layer and the transition layer is observed in all alloys after 8 h of oxidation. At 1000 °C (except WC3009) and 1200 °C, the 8 h oxidized alloys exhibit a clear distinction between the oxide layer and the transition layer. The thickness of the transition layer increases with the increase in temperature and the decrease in Al content. Adding Al does help improve the oxidation resistance, but it is not sufficient to form a dense and protective oxide layer.

ACKNOWLEDGMENTS

X.L. and S.G. acknowledge the financial support from the Swedish Research Council (Grant No. 2019-03559), and the work was also partially supported by the Special International Cooperation Project of Jiangxi Province, China (No. 20232BBH80008).

AUTHOR DECLARATIONS

Conflict of Interest

The authors have no conflicts to disclose.

Author Contributions

Xiaolong Li: Conceptualization (equal); Data curation (equal); Formal analysis (equal); Investigation (equal); Methodology (equal); Validation (equal); Visualization (equal); Writing – original draft (equal). **Yufei Zhao:** Data curation (equal); Formal analysis (equal); Investigation (equal); Validation (equal); Visualization (equal); Writing – review & editing (equal). **Linwei Zhang:** Writing – review & editing (equal). **Qiang Hu:** Writing – review & editing (equal). **Huahai Mao:** Supervision (equal); Writing – review & editing (equal). **Sheng Guo:** Conceptualization (equal); Formal analysis (equal); Funding acquisition (equal); Project administration (equal); Resources (equal); Supervision (equal); Writing – review & editing (equal).

DATA AVAILABILITY

The data that support the findings of this study are available from the corresponding author upon reasonable request.

REFERENCES

- ¹P. Tsakiroopoulos, *Prog. Mater. Sci.* **123**, 100714 (2022).
- ²J. A. Lemberg and R. O. Ritchie, *Adv. Mater.* **24**(26), 3445–3480 (2012).
- ³O. N. Senkov, S. Gorsse, and D. B. Miracle, *Acta Mater.* **175**, 394–405 (2019).
- ⁴J. H. Perepezko, *Science* **326**, 1068–1069 (2009).
- ⁵F. Schwartzberg, H. Ogden, and R. Jaffee, Defense Metals Information Center, Battelle Memorial Institute (1959), Vol. 114, p. 62.
- ⁶O. Senkov, D. Miracle, and N. R. Philips, *U.S. Patent Application No. 2023/0357903 A1* (9 November 2023).
- ⁷J. Wadsworth, T. G. Nieh, and J. J. Stephens, *Int. Mater. Rev.* **33**(1), 131–150 (1988).
- ⁸R. Smith, *J. Less-Common Met.* **2**(2-4), 191–206 (1960).
- ⁹M. P. Brady, I. G. Wright, and B. Gleeson, *JOM* **52**, 16–21 (2000).
- ¹⁰V. V. Satya Prasad, R. G. Baligidad, and A. A. Gokhale, *Aerospace Materials and Material Technologies*, edited by N. Eswara Prasad and R. J. H. Wanhill (Springer, Singapore, 2017).
- ¹¹W. Klopp, D. Maykuth, C. Sims, and R. Jaffee, Battelle Memorial Inst. No. BMI-1317 (1959).
- ¹²Q. Yang *et al.*, *J. Eur. Ceram. Soc.* **43**(10), 4541–4548 (2023).
- ¹³O. N. Senkov, T. I. Daboiku, W. C. Voellmecke, E. J. Payton, S. J. M. Kuhr, and T. M. Butler, *Int. J. Refract. Met. Hard Mater.* **118**, 106462 (2024).
- ¹⁴O. A. Waseem, U. Auyeskan, H. M. Lee, and H. J. Ryu, *J. Mater. Res.* **33**(19), 3226–3234 (2018).
- ¹⁵J. Jayaraj, P. Thirathipviwat, J. Han, and A. Gebert, *Intermetallics* **100**, 9–19 (2018).